analytica

MDPI

Article

A Label-Free Graphene Oxide-Enhanced Piezoelectric Acoustic Biosensor for *DLX1* Detection

Thita Sonklin [1], Dhanunjaya Munthala [1], Machchhendra Thapa [2], Yanwarut Chiraatthakit [3], Ashish Mathur [4], Sanong Suksaweang [2] and Soodkhet Pojprapai [5,*]

1 Institute of Research and Development (IRD), Suranaree University of Technology, Nakhon Ratchasima 30000, Thailand; thita.sk@sut.ac.th (T.S.); dhanuphy@g.sut.ac.th (D.M.)
2 Institute of Medicine, Suranaree University of Technology, Nakhon Ratchasima 30000, Thailand; d6600655@g.sut.ac.th (M.T.); suksawea@sut.ac.th (S.S.)
3 Research Department, Surazense Co., Ltd., Chaimongkon, Nakhon Ratchasima 30000, Thailand; yan.c@surazense.com
4 Centre for Interdisciplinary Research and Innovation (CIDRI), University of Petroleum and Energy Studies, Dehradun 248007, India; ashish.mathur@ddn.upes.ac.in
5 School of Ceramic Engineering, Institute of Engineering, Suranaree University of Technology, Nakhon Ratchasima 30000, Thailand
* Correspondence: soodkhet@g.sut.ac.th; Tel.: +66-4422-4542

Abstract

Distal-less homeobox 1 (*DLX1*) has emerged as a promising urinary biomarker for prostate cancer. This study developed a label-free piezoelectric acoustic biosensor for selective *DLX1* detection using a quartz crystal microbalance (QCM). The QCM gold electrode was sequentially functionalized with L-cysteine, graphene oxide (GO), and an amine-terminated *DLX1* capture probe covalently immobilized through EDC–NHS-mediated amide bond formation. Stepwise surface functionalization was characterized by X-ray photoelectron spectroscopy (XPS), supported by contact angle measurements, X-ray diffraction, and field-emission scanning electron microscopy. XPS provided multi-element evidence for Au–S thiolate formation, GO deposition, amide coupling, probe immobilization, and Watson–Crick hybridization with the synthetic *DLX1* target. Under optimized conditions, the biosensor exhibited a linear response to *DLX1* concentrations and achieved a limit of detection of 81.19 nM. Non-complementary sequences, including *PCA3* and *SARS-CoV-2*, produced frequency shifts below 9 Hz, confirming high selectivity. Comparative experiments showed that GO-mediated covalent immobilization was essential for reliable detection, whereas direct DNA attachment to bare Au generated anomalous positive frequency shifts, which were attributed to weak physisorption. The proposed platform offers a sensitive and selective strategy for quantitative *DLX1* detection and may support future point-of-care nucleic acid diagnostics.

Keywords: *DLX1*; prostate cancer; quartz crystal microbalance; piezoelectric biosensor; graphene oxide; label-free detection; DNA hybridization

Academic Editor: Chiara Zanardi

Received: 25 July 2026
Revised: 27 August 2026
Accepted: 2 September 2026
Published: 4 September 2026

1. Introduction

Understanding biomolecule-nanomaterial interactions is fundamental to the development of biomedical interfaces because surface chemistry governs biomolecular adsorption, stability, accessibility, and recognition. These interactions are particularly important in drug discovery [1], biosensor development [2,3], implants [4], and broader applications in

human healthcare [5,6]. In nucleic-acid biosensors, surface immobilization is especially critical because the attachment of capture probes directly influences their stability, accessibility, and target-recognition efficiency [7].

Graphene-based materials have become especially attractive platforms for biosensing [8–10], owing to their mechanical strength, large surface area, chemical stability, biocompatibility, and ease of functionalization [11]. Graphene oxide (GO) stands out among them: as a two-dimensional, oxygen-rich carbon material, it offers distinct physicochemical properties compared with pristine graphene [12], and its abundant functional groups support both covalent and non-covalent surface modifications that improve specificity and stability in biosensing applications [13]. Combined with low production cost, scalability, and tunable surface chemistry, these properties have driven its use in drug delivery, immobilized catalysis, and healthcare technologies [14].

Reliable biomarker detection remains central to early cancer diagnosis and disease monitoring. Prostate cancer (PCa) is among the most common cancers in men worldwide, ranking as the second most frequently diagnosed cancer in men across more than half the world's countries and territories (112 of 185), with an estimated 1.4 million new cases reported in 2020 [15,16]. Current screening still relies largely on well-known prostate-specific antigen (PSA) testing, but PSA is sensitive without being specific: benign conditions such as prostate enlargement or inflammation can elevate it just as malignant disease does, producing false positives that lead to overdiagnosis, missed aggressive tumors, and unnecessary biopsies, with real physical and psychological costs to patients [17]. These limitations have encouraged the investigation of molecular biomarkers such as *PCA3*, *HOXC6*, *DLX1*, and *KLK3* [18,19]. Among these, distal-less homeobox 1 (*DLX1*) has emerged as a promising candidate because its expression is elevated in malignant prostate tissue and has been associated with tumor progression and metastatic potential [20–22].

Clinical analysis of such transcript biomarkers typically relies on reverse transcription–polymerase chain reaction (RT-PCR), which enables detection of low-abundance circulating and urinary nucleic acids through enzymatic amplification. Although highly sensitive, RT-PCR-based workflows generally require multiple sample-preparation steps, specialized instrumentation, relatively long processing times, and trained personnel. These practical constraints have motivated continued interest in alternative transduction strategies capable of directly converting molecular recognition events into measurable signals.

Alternative biosensing strategies based on electrochemical, optical, and acoustic transduction have therefore been widely investigated for nucleic-acid detection [23–29]. These platforms differ in analytical sensitivity, assay complexity, signal-generation mechanisms, instrumentation requirements, and probe-immobilization strategies. Electrochemical biosensors can achieve low detection limits but often rely on redox labels or signal-amplification schemes, whereas optical methods provide high sensitivity but generally require more sophisticated instrumentation. In contrast, quartz crystal microbalance (QCM) sensors enable direct monitoring of adsorption and hybridization events through resonance-frequency shifts associated with changes in surface-bound mass [24,30,31]. However, their analytical response is strongly governed by the physicochemical properties of the sensing interface, particularly the stability, accessibility, and surface density of immobilized capture probes. Accordingly, interfacial engineering and chemical characterization are critical for improving the performance and mechanistic interpretation of QCM-based nucleic-acid biosensors.

GO has previously been employed for nucleic-acid immobilization in biosensing systems [8,32–34]. Therefore, neither QCM-based gene sensing nor the use of GO for DNA immobilization constitutes novelty in isolation. A remaining challenge is the detailed

characterization of the sequential interfacial reactions involved in biosensor construction and the experimental assessment of the functional contribution of the GO layer.

In the present study, we report a GO-functionalized QCM biosensor for label-free detection of a synthetic *DLX1* oligonucleotide target. The sensing interface was constructed through sequential L-cysteine modification, GO deposition, EDC-NHS activation, and covalent immobilization of an amine-terminated *DLX1* capture probe. GO served as a functional intermediate layer that provided carboxyl-containing groups for EDC-NHS-mediated coupling. The surface-functionalization pathway was systematically investigated using XPS, with changes in Au, S, C, O, N, and P signals providing chemical evidence for Au–S bond formation, GO deposition, amide coupling, probe immobilization, and subsequent target hybridization. Surface morphology, roughness, wettability, and structure were further characterized using FE-SEM, AFM, contact angle analysis, and XRD, respectively. The functional contribution of the GO layer was assessed by comparison with direct probe immobilization on bare Au-QCM. The developed biosensor was evaluated through real-time concentration-dependent measurements, sequence-specificity analysis, and target-binding assessment using Langmuir and Freundlich isotherm models.

2. Materials and Methods

Quartz crystal microbalance (QCM) sensors with a fundamental resonance frequency of 10 MHz (Figure 1a) were purchased from Shenzhen RenLux Crystal Co., Ltd. (Shenzhen, China). Each QCM sensor consisted of an AT-cut quartz wafer (13.9 mm diameter, 160 μm thickness) with 6 mm diameter gold electrodes (200 nm Au over 10 nm Ti adhesion layer) deposited on both the top and bottom surfaces. Piranha solution was prepared by mixing concentrated sulfuric acid (H_2SO_4, 96%, ANaPURE, Auckland, New Zealand) and hydrogen peroxide (H_2O_2, 30%, QReC, Auckland, New Zealand) in a 70:30 (v/v) ratio. Absolute ethanol (99.9%) was obtained from Merck (Darmstadt, Germany). Graphene oxide (GO) as an aqueous dispersion (0.5 mg mL−1) was supplied by Haydale Technologies (Thailand) Company Limited (Pathum Thani, Thailand). 1-ethyl-3-(3-dimethylaminopropyl)carbodiimide hydrochloride (EDC), N-hydroxysuccinimide (sulfo-NHS), Tris-EDTA (TE) buffer, and L-cysteine (L-cys) were purchased from NPChemicals (Bangkok, Thailand). All DNA oligonucleotides were synthesized and HPLC-purified by Utobio (Bangkok, Thailand). The 20-mer *DLX1* capture probe (5′-CGAGTTGACGTAGGGGTAGC-3′) was designed to hybridize with a specific region of Homo sapiens *DLX1* mRNA corresponding to nucleotides 401–420 of the reference sequence (GenBank accession no. AY257976.1). The corresponding synthetic *DLX1* target sequence (5′-GCTACCCCTACGTCAACTCG-3′) was selected based on the sequence reported by Tan et al. (2021) [35]. Non-target control sequences were *PCA3* (5′-GGAAGCACAGAGATCCCTGGG-3′) [36] and *SARS-CoV-2* (5′-CTTGCAAAACCAGACTAAGCTCAT-3′) [2]. The *DLX1* capture probe was amino-terminated (NH_2) to facilitate covalent coupling to the GO surface. The non-target sequences were used to evaluate biosensor selectivity. All oligonucleotide stock solutions were prepared in nuclease-free water and stored at −20 °C. Non-targets were used to assess biosensor selectivity. All DNA stock solutions were prepared in nuclease-free water and stored at −20 °C.

2.1. Fabrication of GO-Coated QCM Electrodes

QCM electrode surfaces were cleaned by immersion in piranha solution (70% H_2SO_4, 30% H_2O_2) for 5 min at room temperature (25 ± 2 °C), followed by thorough rinsing with acetone, absolute ethanol, and deionized (DI) water. Electrodes were air-dried at room temperature for 30 min. To introduce Au-S functional groups on the electrode surface, clean

QCM sensors were immersed in a 10 mmol L^{-1} L-cysteine (L-Cys) aqueous solution for 12 h at room temperature. This L-cysteine self-assembled monolayer served as an adhesion layer for graphene oxide. Graphene oxide (2 mg mL^{-1} stock concentration) was diluted to 0.5 mg mL^{-1} in DI water and sonicated for 10 min to ensure homogeneous dispersion. The L-Cys -coated QCM electrode was subsequently coated with GO using a spin-coating process (500 rpm for 10 min, followed by 6000 rpm for 30 s at room temperature) to form a uniform GO film across the entire electrode surface (Figure 1b). The GO-coated electrode was immersed in DI water overnight to remove weakly bound GO, followed by five sequential rinses with fresh DI water to ensure complete removal of unbound GO particles. The electrodes were then air-dried under laminar flow. To immobilize DNA capture probes, the GO/QCM electrodes were activated by immersion in a solution containing 5 mM EDC and 5 mM sulfo-NHS in DI water for 180 min, the activation time determined to maximize cross-linking efficiency. After activation, the electrodes were rinsed five times with DI water and immediately used for DNA probe attachment.

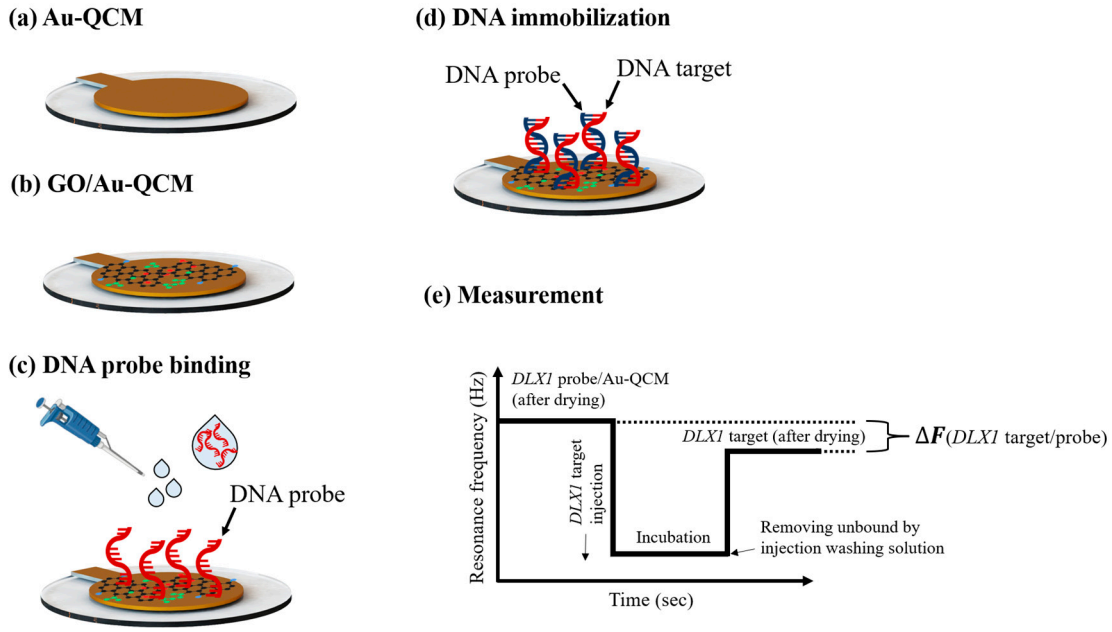

Figure 1. Schematic illustration of (**a**) bare Au-QCM, (**b**) GO/L-Cys surface modification and EDC–NHS activation, (**c**) *DLX1* capture-probe immobilization, (**d**) hybridization with complementary *DLX1* target DNA, and (**e**) Measurement of the QCM frequency response following target DNA hybridization.

2.2. DNA Probe Immobilization and Hybridization

An amino-terminated *DLX1* capture probe was applied to the activated GO-QCM electrode and incubated to allow covalent coupling through amide bond formation between the probe's amino group and the electrode's activated carboxyl groups (Figure 1c). Following incubation, unbound DNA was removed by three sequential washes with 0.1X TE buffer and DI water. Electrodes were then air-dried and denoted as Probe-GO-QCM.

Hybridization experiments (Figure 1d) were performed using target ssDNA sequences diluted to the desired concentrations (10 nM–20 µM) in 1× TE buffer, prepared by a 1:100 dilution of the commercial 100× TE stock solution with nuclease-free water. TE buffer was selected to maintain a stable pH and preserve oligonucleotide integrity during hybridization. Both complementary *DLX1* target sequences and non-complementary control sequences (*PCA3* and *SARS-CoV-2*) were incubated on the probe-functionalized GO-QCM electrodes to allow hybridization with the immobilized capture probe. For each

concentration, measurements were conducted in triplicate (n = 3) using independently prepared electrodes.

2.3. Characterizations

The frequency response of the QCM was measured before and after immobilization using a portable QCM instrument (Surazense Co., Ltd., Nakhon Ratchasima, Thailand) connected to a commercial measurement chamber (Novaetech S.r.l., Pompei, Italy), with a custom-designed electronic module developed at Suranaree University of Technology (Nakhon Ratchasima, Thailand). All measurements were performed under a controlled temperature of 25 °C, monitored with a calibrated thermometer. Frequency data were recorded continuously throughout the hybridization process and for an additional 30–45 min afterward, following removal of unbound molecules. Measurements were taken in two phases: during the hybridization reaction in liquid phase, and after rinsing and drying (Figure 1e). This dual-phase measurement approach enabled assessment of both kinetic association (real-time frequency shift during binding) and equilibrium binding affinity. The resonance-frequency shift at each concentration was recorded following hybridization and rinsing, then plotted against target concentration to generate a curve.

The resonance-frequency shift and mass sensitivity of the QCM can be determined using Sauerbrey's equation, which is expressed as follows:

$$\Delta f = -\frac{2f_0^2 \Delta m}{(\mu_q \rho_q)^{\frac{1}{2}} A} \quad (1)$$

where f_0 is the resonance frequency (Hz), Δf is the change in resonance frequency, Δm is the mass change (g), A is the active surface area of the QCM electrodes (cm^2), p_q is the density of quartz (2.648 g cm^{-3}), and μ_q is the shear modulus of quartz (for AT-cut quartz, $\mu_q = 2.947 \times 10^{11}$ g $cm^{-1}s^{-2}$).

Surface morphology and roughness were characterized using field-emission scanning electron microscopy (FE-SEM; JEOL JSM-6010LV, JEOL Ltd., Akishima, Japan) and atomic force microscopy (AFM; Park NX20, Park Systems Corp., Gwacheon, Republic of Korea), respectively. Surface wettability was evaluated by contact angle analysis. Graphene oxide deposition was examined by X-ray diffraction (XRD; Bruker D8 Advance, Bruker AXS GmbH, Karlsruhe, Germany). The sequential chemical modification of the sensing interface was characterized by X-ray photoelectron spectroscopy (XPS; PHI 5000 VersaProbe II, ULVAC-PHI, Inc., Chigasaki, Japan) at Beamline 3.1, Synchrotron Light Research Institute (SLRI), Nakhon Ratchasima, Thailand. Detailed characterization conditions and instrumental parameters are provided in Section S1.

3. Results

3.1. XRD Analysis

X-ray diffraction (XRD) was used to confirm graphene oxide deposition on the QCM electrode by comparing bare and GO-coated surfaces. Both samples exhibited the characteristic Au/Ti diffraction peaks at 2θ corresponding to the (111) and (311) crystal planes, with the (111) reflection dominating the pattern in each case (Figure 2); the persistence of these peaks after GO coating confirms that the underlying gold electrode structure remains intact and is not disrupted by the deposition process. Only the GO-coated electrode displayed an additional broad diffraction peak centered at $2\theta \approx 11.2^\circ$, corresponding to the (001) reflection of graphene oxide. This peak was absent from the bare QCM pattern.

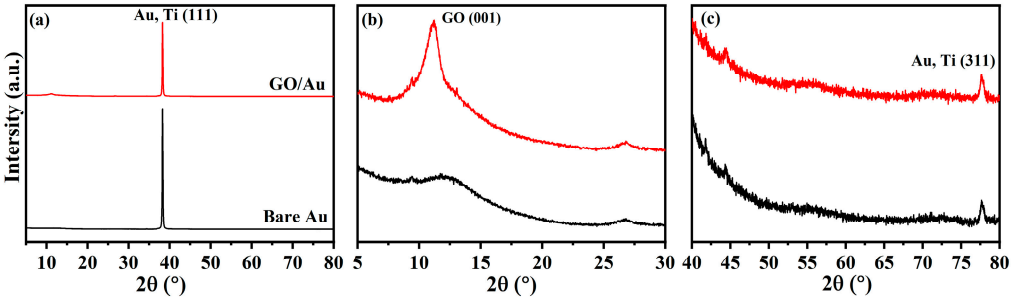

Figure 2. XRD patterns of bare Au-QCM (black line) and GO/Au-QCM (red line): (**a**) full scan, (**b**) enlarged view of the 2θ range from 5° to 30°, and (**c**) enlarged view of the 2θ range from 40° to 80°.

3.2. SEM Images

Field-emission SEM images (Figure 3a) of the bare Au electrode revealed a densely packed, granular morphology typical of polycrystalline gold, with well-defined grain boundaries and a relatively uniform surface texture. Following GO deposition (Figure 3b), the electrode surface morphology changed markedly: the underlying granular gold structure was no longer visible, replaced by smooth, sheet-like domains exhibiting numerous folds and wrinkles, consistent with successful and complete coverage by graphene oxide. Low-magnification imaging (inset, Figure 2b) further confirmed the characteristic wrinkled-sheet morphology of GO. These observations indicate that the spin-coating process produced a continuous GO film.

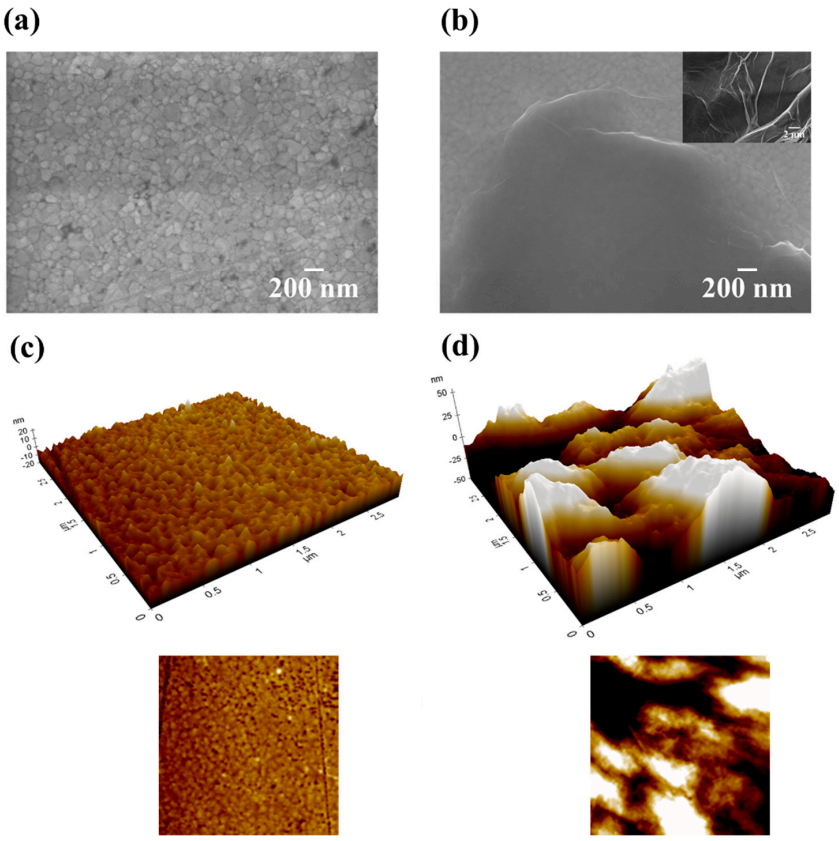

Figure 3. Comparison of surface morphology between bare Au-QCM and GO/Au-QCM characterized by SEM and AFM: (**a**) bare Au-QCM (SEM), (**b**) GO/Au-QCM (SEM), with an inset showing a higher-magnification image of the GO surface, (**c**) bare Au-QCM (AFM), and (**d**) GO/Au-QCM (AFM). The color scale represents variations in surface height, with lighter colors indicating higher regions and darker colors indicating lower regions.

3.3. AFM Images

AFM topography supported these observations (Figure 3c,d; Table 1). The bare Au electrode displayed a uniformly grainy surface with low relief, consistent with the SEM morphology, and an RMS roughness of 0.0037 µm. After GO coating, the surface exhibited substantially greater height variation, replacing the fine granular texture of the bare electrode. This consisted of GO sheets draping over the underlying gold surface. The RMS roughness increased to 0.0142 µm.

Table 1. AFM surface roughness parameters.

Sample	Roughness Average (µm)	Root-Mean-Squared Roughness (µm)
Bare Au-QCM	0.0029	0.0037
GO-QCM	0.0142	0.0185

3.4. GO-QCM Stability Assessment

To evaluate the stability of the GO coating on the electrode surface, the GO-coated Au-QCM was mounted in the measurement chamber equipped with an open holder. DI water was repeatedly introduced onto the electrode surface by pipetting through the open holder (Figure 4a). After each measurement cycle, the resonance frequency was recorded once the signal reached a stable baseline. The reported frequency value was obtained by averaging the signal over a 3 min stabilization period. Across four consecutive measurement cycles, the mean resonance frequency was 10,009,548 Hz with a standard deviation of 4.30 Hz, as provided in Section S2 (Table S1).

3.5. Contact Angle Analysis of Au-QCM Electrodes During Surface Functionalization

Before biomolecule immobilization, contact angle (CA) measurements were performed to evaluate changes in the wettability of the Au-QCM electrode surface following each chemical treatment. Surface wettability reflects the affinity between a solid surface and a liquid and is commonly classified as hydrophobic or hydrophilic, with the extreme cases referred to as superhydrophobic and superhydrophilic, respectively. According to wettability theory, it is based on CA measurement, which is strongly influenced by liquid surface tension [37]. The relationship between CA and the surface tension is described by Young's equation, which can be expressed as follows:

$$cos\theta = \frac{\gamma_{SG} - \gamma_{SL}}{\gamma_{LG}} \quad (2)$$

where γ_{SG}, γ_{SL}, and γ_{LG} are solid–vapor, solid–liquid, and liquid–vapor interfacial tensions, respectively, and θ represents the CA. The equilibrium among these three interfacial tensions determines the contact angle of a liquid droplet on a solid surface.

The surface is considered hydrophobic when the contact angle exceeds 90° and hydrophilic when it is below 90°. Surfaces with contact angles greater than 150° and less than 50° are classified as superhydrophobic and superhydrophilic, respectively [38]. Surface wettability is an important parameter in biosensor design because hydrophilic surfaces promote favorable interactions between immobilized bioreceptors and target analytes [39]. Based on our previous work [40], the untreated Au-QCM surface exhibited a contact angle of 69°. In the present study (Figure 4b), after piranha cleaning, the contact angle decreased to 45.38 ± 0.90°, which indicated enhanced surface hydrophilicity. Subsequent modification with L-cysteine further reduced the contact angle to 41.24 ± 1.17°. After GO coating, the contact angle remained relatively unchanged at 40.44 ± 0.51°. Further activation with

EDC/NHS reduced the contact angle to 36.91 ± 0.27°. Probe immobilization produced the lowest contact angle of 31.89 ± 3.64°. The increased hydrophilicity observed after piranha treatment is likely attributed to the formation of hydroxyl-rich surface species on the Au surface [41]. The further decrease in contact angle after L-cysteine modification, EDC/NHS activation, and probe immobilization indicated the introduction of additional polar functional groups onto the electrode surface. Although GO deposition caused only a minor change in contact angle, the surface remained highly hydrophilic. The progressive reduction in contact angle from 69° (pristine Au) to 31.89° (probe-modified surface) across all modification stages confirms the surface functionalization of the Au-QCM electrode. The resulting highly hydrophilic interface is expected to facilitate effective biomolecule immobilization and promote favorable analyte interaction during *DLX1* target detection.

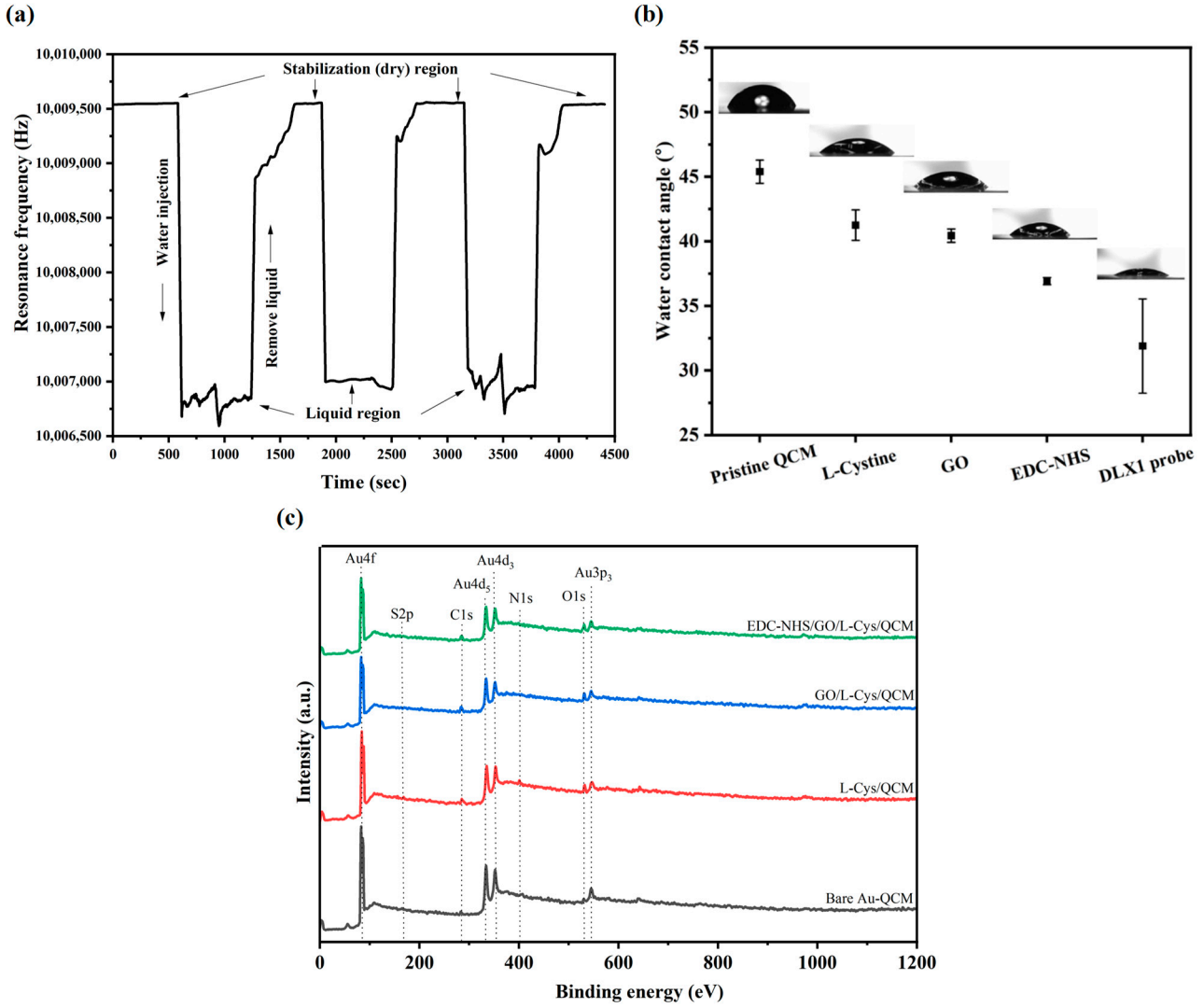

Figure 4. Surface stability and physicochemical characterization of the functionalized Au-QCM electrode: (**a**) repeated DI-water injection for evaluation of GO-coating stability; (**b**) contact angle measurements during sequential surface functionalization; and (**c**) XPS survey spectra at different stages of surface modification.

3.6. XPS Analysis

XPS analysis was performed to verify the sequential chemical modification of the Au-QCM sensing interface. The survey spectra (Figure 4c) and elemental compositions (Table 2) showed systematic changes following L-cysteine immobilization, GO deposition, and EDC–NHS activation. L-cysteine modification was supported by changes in the Au

and S signals associated with Au–S bonding and GO deposition increased the contribution of carbon- and oxygen-containing species. Subsequent EDC–NHS activation produced pronounced changes in the nitrogen and carbon signals, consistent with formation of an activated surface for subsequent coupling of the amino-terminated *DLX1* capture probe. Collectively, these results support the sequential formation of the L-Cys/GO/EDC–NHS sensing interface. Detailed high-resolution XPS spectra, peak assignments, and fitting parameters are provided in Section S3 (Figure S1 and Tables S2–S5).

Table 2. XPS atomic percentage analysis.

Name	Atomic %				
	Au 4f	**S 2P**	**C 1S**	**N 1S**	**O 1S**
Bare Au	31.09	20.86	20.37	-	17.38
L-Cys/Au	25.09	44.40	22.56	38.72	33.75
GO/L-Cys/Au	19.93	18.87	28.25	4.36	25.11
EDC-NHS/GO/L-Cys/Au	23.89	15.88	28.81	56.92	23.76

3.7. Evaluation of GO and EDC/NHS Coupling in Probe Immobilization

To evaluate the contribution of GO and EDC/NHS coupling to biosensor performance, a comparative study was conducted using a bare Au-QCM surface without GO modification. In this case, *DLX1* probe immobilization was attempted directly on the gold surface. Although direct attachment of DNA onto unmodified gold surfaces has been reported through electroactive surface sites, the limited number of reactive functional groups generally restricts probe immobilization efficiency [42]. The corresponding frequency response profiles are presented in Figure 5a,b.

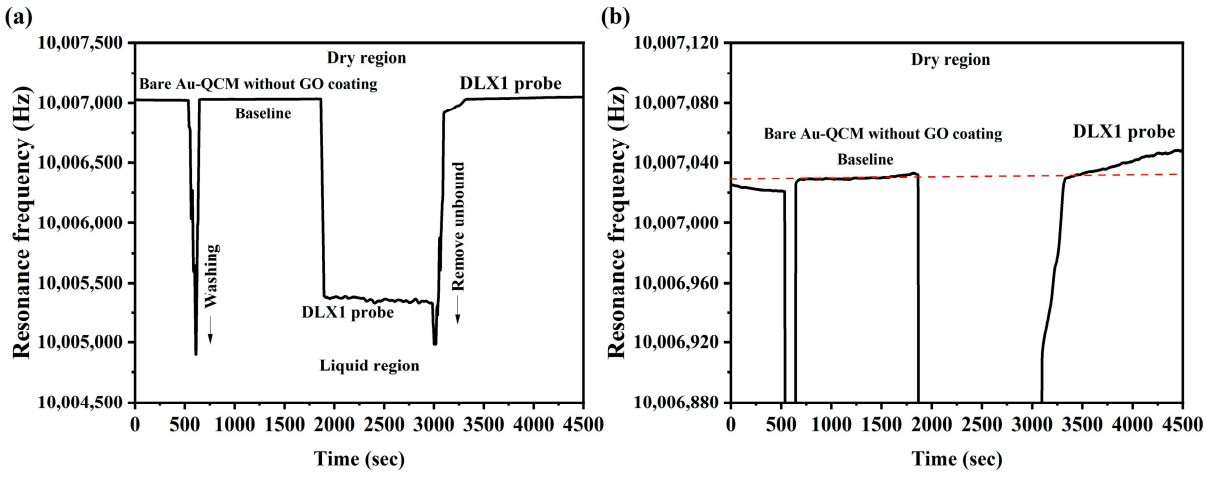

Figure 5. *DLX1* probe immobilization on bare Au-QCM without graphene oxide coating: (**a**) real-time response and (**b**) enlarged dry-region response. The red dashed line indicates the baseline resonance frequency used as the reference.

Upon introduction of the *DLX1* probe onto the bare Au-QCM surface, a positive resonance-frequency shift was observed instead of the expected negative shift associated with mass loading. This phenomenon is known as anti-Sauerbrey behavior [43]. The absence of covalent attachment between the *DLX1* probe and the bare Au surface resulted in weak, non-specific DNA physisorption, which formed a soft and loosely coupled interfacial layer. The poor interaction between the DNA probe and the bare gold surface allowed the adsorbed molecules to move independently rather than oscillate synchronously with

the quartz crystal, thereby producing the observed anti-Sauerbrey positive frequency response. In contrast, the GO-modified biosensor exhibited a well-defined negative frequency shift under identical conditions, consistent with covalent probe immobilization through EDC/NHS coupling. This stable attachment ensured synchronous oscillation of the probe layer with the quartz crystal and maintained the system within the valid Sauerbrey regime, as shown in Figure 6.

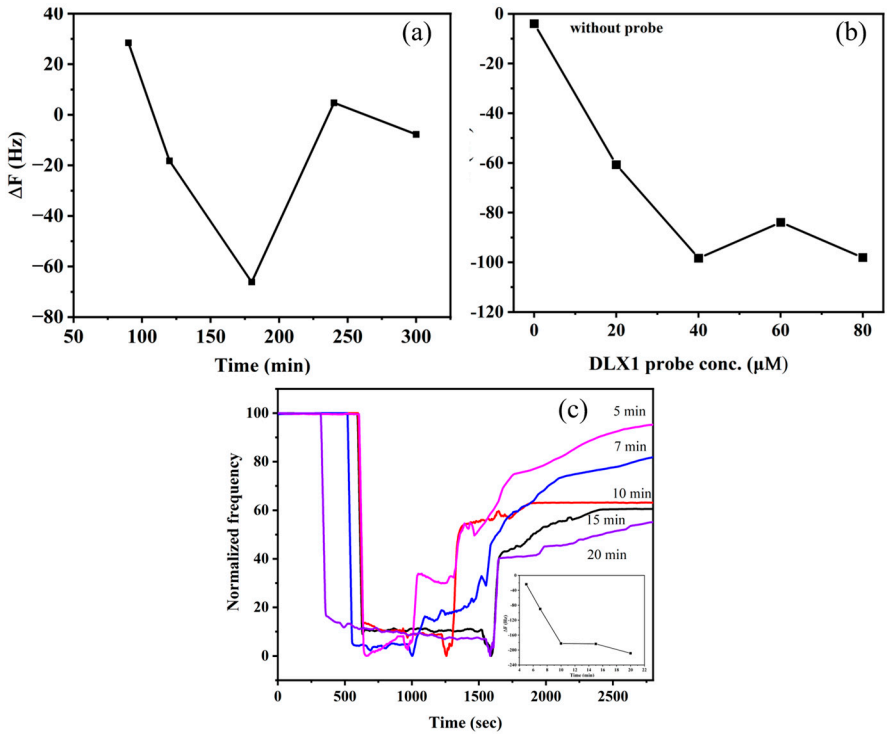

Figure 6. Optimization of (**a**) EDC/NHS activation time, (**b**) *DLX1* capture probe concentration, and (**c**) *DLX1* target hybridization time.

3.8. Optimization Studies

Several key parameters, including EDC/NHS activation time, capture probe concentration, and target hybridization time, were optimized to achieve the best sensor performance, as shown in Figure 6. The first parameter examined was the EDC/NHS activation time for the carboxyl groups on the GO-coated QCM surface. Activation times ranging from 90 to 300 min were evaluated at 60 min intervals. As shown in Figure 6a, the frequency shift increased with activation time and reached a maximum at 180 min. Beyond this point, no further improvement was observed. Therefore, 180 min was selected as the optimum activation time for subsequent experiments. The effect of probe concentration was then investigated over a range of 0–80 nM. As shown in Figure 6b, the resonance-frequency shift increased as probe concentration increased and reached a plateau at 40 μM. This result suggests that the available binding sites on the electrode surface became sufficiently occupied at this concentration. Therefore, 40 μM was selected as the optimum probe concentration for all subsequent studies. The hybridization time required for target recognition was optimized with 10 nM *DLX1* target DNA. Figure 6c presents the normalized frequency response at hybridization times between 5 and 20 min. The resonance-frequency shift increased up to 10 min and remained nearly constant thereafter, which suggested that hybridization had reached equilibrium. Therefore, 10 min was selected as the optimum hybridization time for target recognition because it produced the maximum sensor response with the shortest assay time.

3.9. DLX1 Detection

The normalized resonance-frequency responses of the *DLX1* probe/EDC–NHS/GO/L-Cys/Au-QCM biosensor over the concentration range of 10 nM–20 µM are provided in Section S4 (Figures S2 and S3). Figure S2 presents the full response profiles, whereas Figure S3 provides magnified views of the drying region. For each concentration, S1–S3 represent three independently prepared QCM sensors (n = 3).

The *DLX1* probe/EDC–NHS/GO/L-Cys/Au-QCM surface was exposed to the DLX1 target solution for 10 min, followed by rinsing to remove unbound and weakly adsorbed molecules. Hybridization between the immobilized probe and the complementary target resulted in increased surface-associated mass. After rinsing, the signals recovered due to the removal of residual liquid and unbound or weakly adsorbed molecules from the sensor surface. The remaining stable frequency shift reflects the mass contribution of specifically hybridized DLX1 target molecules and serves as the analytical signal for target detection. At lower target concentrations (10–100 nM), relatively small residual responses were observed. At higher target concentrations, larger-magnitude negative responses were obtained, consistent with increased target binding and surface mass loading. Variations among S1–S3 were observed mainly during the hybridization and washing stages and may reflect differences in liquid handling, mass transport, and individual sensor-surface preparation.

The resonance-frequency shift is shown in Figure 7. Figure 7a shows the full concentration–response curve of the biosensor across the tested *DLX1* concentration range. The resonance-frequency shift increased with *DLX1* target concentration and reached saturation at approximately 65 Hz beyond 10 µM, consistent with surface saturation at high target concentrations. To further characterize the concentration-dependent binding response, the resonance-frequency shifts were analyzed by nonlinear regression using the Langmuir and Freundlich isotherm models [44–46]. The Langmuir model describes a saturable surface-binding response in which a finite number of accessible binding sites are progressively occupied as the target concentration increases:

$$\Delta f = \frac{\Delta f_{max} C}{K_D + C} \quad (3)$$

where Δf is the resonance-frequency shift at *DLX1* concentration C, Δf_{max} is the fitted maximum frequency shift, and K_D is the apparent dissociation constant. By definition, in this form of the model, the predicted response reaches one-half of Δf_{max} when $C = K_D$. The Langmuir fit yielded a Δf_{max} of 62.08 Hz and an apparent K_D of 0.39 µM, with R^2 = 0.95. Thus, the fitted K_D indicates that the predicted half-maximal QCM response occurs at a *DLX1* concentration of approximately 0.39 µM. The fitted response increased rapidly at lower concentrations and gradually approached a plateau at higher concentrations, consistent with the experimentally observed concentration–response profile.

The same data were also fitted using the Freundlich model:

$$\Delta f = K_F C^{\frac{1}{n}} \quad (4)$$

where K_F is the Freundlich response constant and 1/n is the heterogeneity exponent. The Freundlich fit yielded K_F = 38.87 and $\frac{1}{n}$ = 0.23, with R^2 = 0.94. Comparison of the two models (Table 3) showed that the Langmuir model provided a slightly better fit than the Freundlich model. In addition, the Δf_{max} of 62.08 Hz was close to the maximum experimental response. These results indicate that the Langmuir model provides a slightly better description of the concentration-dependent interaction between the *DLX1* target and the immobilized capture probe on the functionalized QCM surface under the investigated conditions.

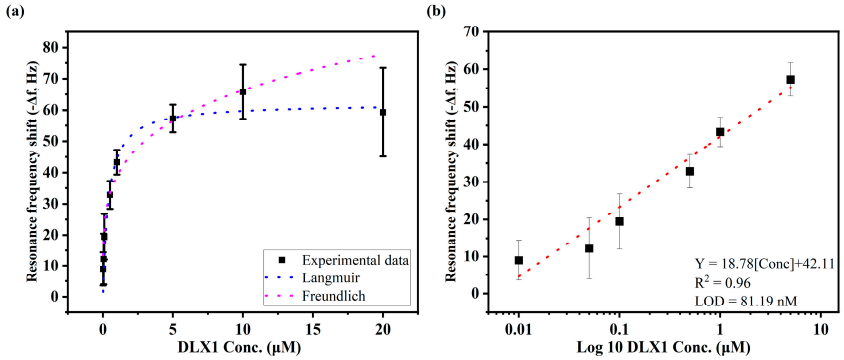

Figure 7. *DLX1* target detection using the *DLX1* probe/EDC–NHS/GO/L-Cys/Au-QCM biosensor: (**a**) concentration-dependent resonance-frequency shifts over the range of 10 nM–20 μM, with nonlinear fitting using the Langmuir and Freundlich isotherm models; and (**b**) a semi-logarithmic calibration plot with linear regression.

Table 3. Langmuir and Freundlich isotherm model parameters and correlation coefficients.

Langmuir			Freundlich		
ΔF_{max} (Hz)	K_D (μM)	R^2	K_F	$\frac{1}{n}$	R^2
62.08 ± 3.83	0.39 ± 0.09	0.95	38.87 ± 1.94	0.23	0.94

The limit of detection (*LOD*) was calculated as follows [47]:

$$LOD = \frac{\sigma}{S} \quad (5)$$

where σ is the standard deviation of the response and S is the sensitivity factor, calculated as 0.13 × the slope of the semi-logarithmic calibration curve. Figure 7b shows the linear calibration obtained by plotting the resonance-frequency shift against the logarithm of the *DLX1* concentration. A strong linear relationship was obtained (R^2 = 0.99), with an estimated *LOD* of 81.19 nM. Although this *LOD* demonstrates measurable detection of synthetic *DLX1* targets under the investigated conditions, it remains substantially higher than the attomolar-to-femtomolar concentrations expected for *DLX1* transcripts in unprocessed clinical urine or plasma. Therefore, the current platform is not sufficiently sensitive for amplification-free detection in clinical samples. Further improvements in analytical sensitivity will require either upstream nucleic acid amplification or enhanced QCM mass sensitivity. Potential strategies include the use of higher-frequency QCM crystals and mass-amplification approaches, such as sandwich assays employing gold-nanoparticle-labeled reporter probes. These approaches may further improve the detection limit while retaining the label-free acoustic sensing principle.

Table 4 summarizes the measured resonance-frequency shifts and corresponding surface mass densities calculated using the Sauerbrey relationship to estimate *DLX1* loading on the probe-functionalized QCM surface. As the *DLX1* concentration increased from 0.01 to 10 μM, the frequency shift increased from 8.98 to 65.80 Hz, corresponding to an increase in surface mass density from 39.75 to 291.18 ng cm^{-2}. The highest surface mass density was observed at 10 μM. At 20 μM, the frequency shift decreased to 59.31 Hz, corresponding to a surface mass density of 262.47 ng cm^{-2}. These results indicate that no further increase in surface loading occurred above 10 μM and that the response had approached a saturation region. The concentration-dependent increase in surface mass is consistent with progressive hybridization of the complementary *DLX1* target with the immobilized capture probes. At lower concentrations, increasing target availability resulted in greater surface loading, whereas at higher concentrations, the response gradually approached a plateau as the accessible probe-binding sites became increasingly occupied. Although the mean response

decreased slightly at 20 μM, the relatively large variability at this concentration should be considered when interpreting this decline. These data support a concentration-dependent response that approaches saturation at higher *DLX1* concentrations.

Table 4. Resonance-frequency shifts and corresponding surface mass densities at different *DLX1* target concentrations.

Conc (μM)	Conc (ng/uL)	ΔF (Hz)	Δ*m* (ng/cm^2)
0.01	0.066	8.98243	39.750171
0.05	0.33	12.19024	53.945772
0.1	0.66	19.43135	85.990036
0.5	3.3	32.85128	145.37759
1	6.6	43.3136	191.67675
5	33	57.28709	253.51398
10	66	65.7982	291.17841
20	132	59.31195	262.47465

3.10. Specificity of DLX1 Hybridization

The specificity of the *DLX1*/probe/EDC-NHS/GO/L-Cys/Au-QCM biosensor was evaluated by exposing the probe-modified surface to non-complementary target sequences, including *PCA3* and *SARS-CoV-2* DNA, at an equivalent concentration of 10 μM. The resonance-frequency shift observed upon introduction of *PCA3* and *SARS-CoV-2* targets was less than 9 Hz in both cases, substantially lower than the frequency change produced by the complementary *DLX1* target (65 Hz) under the same conditions (Figure 8). This minimal response confirms that non-complementary sequences do not undergo stable hybridization with the immobilized *DLX1* probe, as the absence of Watson–Crick base-pair [48] complementarity between the probe and the non-target sequences prevents specific molecular recognition at the biosensor surface. However, the present specificity assessment was conducted using synthetic oligonucleotides, and the effects of complex biological matrices have not yet been established. Components of urine or serum, including proteins, salts, metabolites, and other biomolecules, may contribute to non-specific adsorption, changes in interfacial viscoelasticity, or interference with probe-target hybridization, thereby affecting the QCM frequency response. In addition, specificity against closely homologous sequences, single-base mismatches, and non-target genomic fragments remains to be evaluated. Further studies incorporating homologous and mismatch controls, spiked artificial urine, and biological samples, together with appropriate surface-blocking strategies, are therefore required to assess matrix effects and establish biological specificity before clinical application.

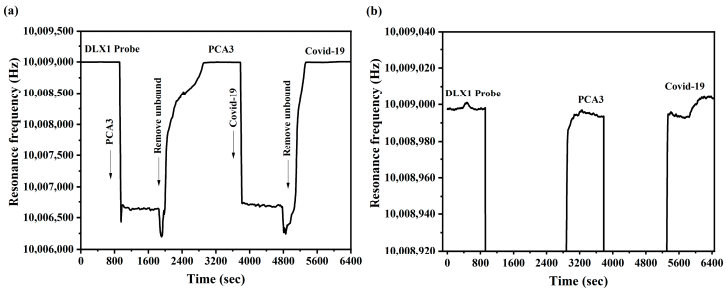

Figure 8. Specificity of the *DLX1* probe/GO/EDC–NHS/L-Cys/Au-QCM biosensor against non-complementary *PCA3* and COVID-19 DNA targets: (**a**) real-time response and (**b**) dry-state frequency response.

4. Conclusions

In summary, this study introduces a novel label-free piezoelectric acoustic biosensor for the selective detection of the *DLX1* prostate cancer biomarker through the sequential assembly of L-cysteine SAM formation, graphene oxide deposition, EDC-NHS covalent activation, and *DLX1* probe immobilization on the Au-QCM electrode surface, thereby establishing a well-defined and chemically stable, functionalized platform. In this approach, the role of GO is central to the performance of the biosensor, as its array of reactive carboxyl groups enables efficient covalent probe attachment through EDC-NHS-mediated amide bond formation, which ensures rigid acoustic coupling between the immobilized probe layer and the quartz crystal and places the system within the valid range of the Sauerbrey mass-loading model. Under optimized conditions (180 min EDC/NHS activation, 40 μM probe concentration, and 10 min hybridization time), the biosensor achieved a limit of detection of 81.19 nM and demonstrated high selectivity, with frequency shifts below 9 Hz for non-complementary *PCA3* and COVID-19 DNA. The combination of GO functionalization and covalent surface chemistry offers a robust and reproducible platform for nucleic acid biosensing and may be readily extended to the detection of other cancer-related biomarkers for future diagnostic and point-of-care applications.

Supplementary Materials: The following supporting information can be downloaded at https://www.mdpi.com/article/10.3390/analytica7030063/s1: Section S1: Detailed Surface Characterization Conditions; Section S2: GO-QCM Stability Assessment; Table S1: Resonance frequency response of the GO-coated Au-QCM during repeated washing with DI water; Section S3: XPS Analysis; Figure S1: XPS spectral fitting at each modification step; Tables S2–S5: XPS fitting parameters of the S 2p, C 1s, N 1s, and O 1s core-level spectra, respectively; Section S4: DLX1 Detection; Figure S2: Normalized resonance frequency responses of the DLX1 probe/EDC–NHS/GO/L-Cys/Au-QCM biosensor at different target concentrations; Figure S3: Magnified views of the normalized resonance frequency responses at different DLX1 target concentrations [49–75].

Author Contributions: Conceptualization, T.S.; methodology, T.S., D.M., M.T. and Y.C.; investigation, T.S., A.M. and S.S.; data curation, T.S.; writing—original draft preparation, T.S.; writing—review and editing, D.M., M.T., Y.C., A.M., S.S. and S.P.; visualization, S.P.; supervision, A.M., S.S. and S.P.; project administration, S.P.; funding acquisition, S.P. All authors have read and agreed to the published version of the manuscript.

Funding: This research was funded by Suranaree University of Technology (SUT), grant number Full-time66/52/2569.

Data Availability Statement: The original contributions presented in this study are included in the article and the Supplementary Materials. Further inquiries can be directed to the corresponding author.

Acknowledgments: The authors gratefully acknowledge Beamline 3.1, Synchrotron Light Research Institute (SLRI), Thailand, for providing access to XPS facilities and technical support. The authors also thank Suranaree University of Technology (SUT) and Surazense Co., Ltd. for providing laboratory facilities and research support. During the preparation of this manuscript, the authors used ChatGPT v.GPT-5.6 Sol (OpenAI, San Francisco, CA, USA) for English-language editing, grammatical correction, and to improve clarity and organization. The authors reviewed and edited the output and take full responsibility for the content of this publication.

Conflicts of Interest: Author Y.C. is affiliated with Surazense Co., Ltd. The company had no role in the design of the study; in the collection, analysis, or interpretation of the data; in the writing of the manuscript; or in the decision to publish the results. The remaining authors declare that the research was conducted in the absence of any commercial or financial relationships that could be construed as a potential conflict of interest.

Abbreviations

The following abbreviations are used in this manuscript:

AFM	Atomic force microscopy
Au-QCM	Gold-coated quartz crystal microbalance
CA	Contact angle
COVID-19	Coronavirus disease 2019
DI	Deionized
DLX1	Distal-less homeobox 1
DNA	Deoxyribonucleic acid
EDC	1-Ethyl-3-(3-dimethylaminopropyl) carbodiimide hydrochloride
FE-SEM	Field-emission scanning electron microscopy
GO	Graphene oxide
GO-QCM	Graphene oxide-coated quartz crystal microbalance
HOXC6	Homeobox C6
HPLC	High-performance liquid chromatography
L-Cys	L-Cysteine
LOD	Limit of detection
NHS	N-Hydroxysuccinimide
PCa	Prostate cancer
PCA3	Prostate cancer antigen 3
PSA	Prostate-specific antigen
QCM	Quartz crystal microbalance
RMS	Root mean square
RT-PCR	Reverse transcription–polymerase chain reaction
SAM	Self-assembled monolayer
SARS-CoV-2	Severe acute respiratory syndrome coronavirus 2
ssDNA	Single-stranded DNA
sulfo-NHS	N-Hydroxysulfosuccinimide
SUT	Suranaree University of Technology
TE	Tris–EDTA
UV	Ultraviolet
XPS	X-ray photoelectron spectroscopy
XRD	X-ray diffraction

References

1. Goenka, S.; Sant, V.; Sant, S. Graphene-based nanomaterials for drug delivery and tissue engineering. *J. Control. Release* **2014**, *173*, 75–88. [CrossRef] [PubMed]
2. Munthala, D.; Sonklin, T.; Chanlek, N.; Mathur, A.; Roy, S.; Avasthi, D.K.; Suksaweang, S.; Pojprapai, S. Portable DNA Probe Detector and a New Dry-QCM Approach for SARS-CoV-2 Detection. *Technologies* **2025**, *13*, 114. [CrossRef]
3. Tongpeng, S.; Weerapakdee, C.; Sonklin, T.; Pojprapai, S.; Jiansirisomboon, S. A Portable QCM-Based Biosensor-Incorporated Graphene Oxide for Point-of-Care Prostate Cancer Marker Detection. *Technologies* **2025**, *13*, 544. [CrossRef]
4. Soe, Z.C.; Wahyudi, R.; Mattheos, N.; Lertpimonchai, A.; Everts, V.; Tompkins, K.A.; Osathanon, T.; Limjeerajarus, C.N.; Limjeerajarus, N. Application of nanoparticles as surface modifiers of dental implants for revascularization/regeneration of bone. *BMC Oral Health* **2024**, *24*, 1175. [CrossRef] [PubMed]
5. Liu, J.; Peng, Q. Protein-gold nanoparticle interactions and their possible impact on biomedical applications. *Acta Biomater.* **2017**, *55*, 13–27. [CrossRef] [PubMed]
6. Kaymaz, S.V.; Nobar, H.M.; Sarıgül, H.; Soylukan, C.; Akyüz, L.; Yüce, M. Nanomaterial surface modification toolkit: Principles, components, recipes, and applications. *Adv. Colloid Interface Sci.* **2023**, *322*, 103035. [CrossRef] [PubMed]
7. Xue, Z.; Wang, L.; Pan, S.; Yan, J.; You, M.; Yao, C. The nucleic acid reactions on the nanomaterials surface for biomedicine. *J. Nanobiotechnol.* **2025**, *23*, 308. [CrossRef] [PubMed]
8. Lee, J.; Kim, J.; Kim, S.; Min, D.-H. Biosensors based on graphene oxide and its biomedical application. *Adv. Drug Deliv. Rev.* **2016**, *105*, 275–287. [CrossRef] [PubMed]

9. Narang, J.; Malhotra, N.; Singhal, C.; Mathur, A.; Chakraborty, D.; Anil, A.; Ingle, A.; Pundir, C.S. Point of care with micro fluidic paper based device integrated with nano zeolite–graphene oxide nanoflakes for electrochemical sensing of ketamine. *Biosens. Bioelectron.* **2017**, *88*, 249–257. [CrossRef] [PubMed]
10. Gutiérrez, J.; Robein, Y.N.; Juan, J.; Di Nezio, M.S.; Pistonesi, C.; González, E.A.; Santos, R.; Pistonesi, M.F. A combined experimental and DFT study on the zero valent iron/reduced graphene oxide doped QCM sensor for determination of trace concentrations of As using a Flow-batch system. *Sens. Actuators B Chem.* **2024**, *404*, 135233. [CrossRef]
11. Ozbey, S.; Keles, G.; Kurbanoglu, S. Innovations in graphene-based electrochemical biosensors in healthcare applications. *Microchim. Acta* **2025**, *192*, 290. [CrossRef] [PubMed]
12. Ababay Ketema, W.; Delele Worku, A. Recent advances of graphene-based materials for emerging technologies. *Results Chem.* **2023**, *5*, 100971. [CrossRef]
13. Ramoso, J.P.; Rasekh, M.; Balachandran, W. Graphene-Based Biosensors: Enabling the Next Generation of Diagnostic Technologies—A Review. *Biosensors* **2025**, *15*, 586. [CrossRef] [PubMed]
14. Yu, W.; Sisi, L.; Haiyan, Y.; Jie, L. Progress in the functional modification of graphene/graphene oxide: A review. *RSC Adv.* **2020**, *10*, 15328–15345. [CrossRef] [PubMed]
15. Bergengren, O.; Pekala, K.R.; Matsoukas, K.; Fainberg, J.; Mungovan, S.F.; Bratt, O.; Bray, F.; Brawley, O.; Luckenbaugh, A.N.; Mucci, L.; et al. 2022 Update on Prostate Cancer Epidemiology and Risk Factors—A Systematic Review. *Eur. Urol.* **2023**, *84*, 191–206. [CrossRef] [PubMed]
16. Manorom, D. Trends and projections in prostate cancer epidemiology in Thailand: A population-based cancer registry analysis. *Asian J. Urol.* **2026**, *13*, 37–44. [CrossRef] [PubMed]
17. Dushimova, Z.; Iztleuov, Y.; Chingayeva, G.; Shepetov, A.; Mustapayeva, N.; Shatkovskaya, O.; Pashimov, M.; Saliev, T. Overdiagnosis and Overtreatment in Prostate Cancer. *Diseases* **2025**, *13*, 167. [CrossRef] [PubMed]
18. Crocetto, F.; Musone, M.; Chianese, S.; Conforti, P.; Digitale Selvaggio, G.; Caputo, V.F.; Falabella, R.; Del Giudice, F.; Giulioni, C.; Cafarelli, A.; et al. Blood and urine-based biomarkers in prostate cancer: Current advances, clinical applications, and future directions. *J. Liq. Biopsy* **2025**, *9*, 100305. [CrossRef] [PubMed]
19. Mytsyk, Y.; Nakonechnyi, Y.; Dosenko, V.; Kowal, P.; Pietrus, M.; Gazdikova, K.; Labudova, M.; Caprnda, M.; Prosecky, R.; Dragasek, J.; et al. The performance and limitations of PCA3, TMPRSS2:ERG, HOXC6 and DLX1 urinary markers combined in the improvement of prostate cancer diagnostics. *Clin. Biochem.* **2023**, *116*, 120–127. [CrossRef] [PubMed]
20. Zhang, D.; Xu, J.; Wang, J.; Jiang, J. Identification of prostate cancer by urinary DLX1/HOXC6 expression in Chinese population with prostate-specific antigen levels of 4–10 ng/mL. *Sci. Rep.* **2025**, *16*, 3293. [CrossRef] [PubMed]
21. Liang, M.; Sun, Y.; Yang, H.L.; Zhang, B.; Wen, J.; Shi, B.K. DLX1, a binding protein of beta-catenin, promoted the growth and migration of prostate cancer cells. *Exp. Cell Res.* **2018**, *363*, 26–32. [CrossRef] [PubMed]
22. Chan, D.W.; Hui, W.W.Y.; Wang, J.J.; Yung, M.M.H.; Hui, L.M.N.; Qin, Y.; Liang, R.R.; Leung, T.H.Y.; Xu, D.; Chan, K.K.L.; et al. DLX1 acts as a crucial target of FOXM1 to promote ovarian cancer aggressiveness by enhancing TGF-β/SMAD4 signaling. *Oncogene* **2017**, *36*, 1404–1416. [CrossRef] [PubMed]
23. Soler, M.; Estevez, M.C.; Cardenosa-Rubio, M.; Astua, A.; Lechuga, L.M. How Nanophotonic Label-Free Biosensors Can Contribute to Rapid and Massive Diagnostics of Respiratory Virus Infections: COVID-19 Case. *ACS Sens.* **2020**, *5*, 2663–2678. [CrossRef] [PubMed]
24. Fam, M.K.; Ismail, N.I.; Zahari, A.I.; Ghazali, N.A.; Hassan, N. Biosensor technologies in cancer: Tools for early detection and prognostic monitoring. *Biomark. Res.* **2025**, *14*, 8. [CrossRef] [PubMed]
25. Erdem, A.; Senturk, H.; Karakus, M. Molecularly imprinted polymer-based sensors: Design and advances in the analysis of DNA and protein. *Talanta Open* **2025**, *12*, 100507. [CrossRef]
26. Szymczyk, A.; Ziółkowski, R.; Malinowska, E. Modern Electrochemical Biosensing Based on Nucleic Acids and Carbon Nanomaterials. *Sensors* **2023**, *23*, 3230. [CrossRef] [PubMed]
27. Xiao, M.; Lai, W.; Man, T.; Chang, B.; Li, L.; Chandrasekaran, A.R.; Pei, H. Rationally Engineered Nucleic Acid Architectures for Biosensing Applications. *Chem. Rev.* **2019**, *119*, 11631–11717. [CrossRef] [PubMed]
28. Sagar Shrikrishna, N.; Sharma, R.; Sahoo, J.; Kaushik, A.; Gandhi, S. Navigating the landscape of optical biosensors. *Chem. Eng. J.* **2024**, *490*, 151661. [CrossRef]
29. Bai, H.; Wang, Y.; Li, X.; Guo, J. Electrochemical nucleic acid sensors: Competent pathways for mobile molecular diagnostics. *Biosens. Bioelectron.* **2023**, *237*, 115407. [CrossRef] [PubMed]
30. Lim, H.J.; Saha, T.; Tey, B.T.; Tan, W.S.; Ooi, C.W. Quartz crystal microbalance-based biosensors as rapid diagnostic devices for infectious diseases. *Biosens. Bioelectron.* **2020**, *168*, 112513. [CrossRef] [PubMed]
31. Fredriksson, C.; Kihlman, S.; Rodahl, M.; Kasemo, B. The Piezoelectric Quartz Crystal Mass and Dissipation Sensor: A Means of Studying Cell Adhesion. *Langmuir* **1998**, *14*, 248–251. [CrossRef]
32. Nair, M.P.; Teo, A.J.T.; Li, K.H. Acoustic Biosensors and Microfluidic Devices in the Decennium: Principles and Applications. *Micromachines* **2022**, *13*, 24. [CrossRef] [PubMed]

33. Liu, X.; Wang, J.-Y.; Mao, X.-B.; Ning, Y.; Zhang, G.-J. Single-Shot Analytical Assay Based on Graphene-Oxide-Modified Surface Acoustic Wave Biosensor for Detection of Single-Nucleotide Polymorphisms. *Anal. Chem.* **2015**, *87*, 9352–9359. [CrossRef] [PubMed]
34. Gao, Y.; Wang, Y. Interplay of graphene–DNA interactions: Unveiling sensing potential of graphene materials. *Appl. Phys. Rev.* **2024**, *11*, 011306. [CrossRef] [PubMed]
35. Tan, G.G.; Xu, C.; Zhong, W.K.; Wang, C.Y. miR-184 delays cell proliferation, migration and invasion in prostate cancer by directly suppressing DLX1. *Exp. Ther. Med.* **2021**, *22*, 1163. [CrossRef] [PubMed]
36. Raj, D.; Wadhwa, S.; Roy, S.; Kumar, A.; Kumar, D.; Kant, K.; Pojprapai, S.; Mathur, A. Affordable ultrasensitive electrochemical detection of PCA3 for early prostate cancer diagnosis. *Sci. Rep.* **2025**, *15*, 33849. [CrossRef] [PubMed]
37. Martinez-Urrutia, A.; Fernandez de Arroiabe, P.; Ramirez, M.; Martinez-Agirre, M.; Mounir Bou-Ali, M. Contact angle measurement for LiBr aqueous solutions on different surface materials used in absorption systems. *Int. J. Refrig.* **2018**, *95*, 182–188. [CrossRef]
38. Wang, P.; Su, J.; Shen, M.; Ruths, M.; Sun, H. Detection of Liquid Penetration of a Micropillar Surface Using the Quartz Crystal Microbalance. *Langmuir* **2017**, *33*, 638–644. [CrossRef] [PubMed]
39. Jandas, P.J.; Luo, J.; Quan, A.; Qiu, C.; Cao, W.; Fu, C.; Fu, Y.Q. Highly selective and label-free Love-mode surface acoustic wave biosensor for carcinoembryonic antigen detection using a self-assembled monolayer bioreceptor. *Appl. Surf. Sci.* **2020**, *518*, 146061. [CrossRef]
40. Sonklin, T.; Tongpeng, S.; Munthala, D.; Suksaweang, S.; Janphuang, P.; Bharti, A.; Mathur, A.; Avasthi, D.K.; Jiansirisomboon, S.; Pojprapai, S. Development of gold nanospikes-modified quartz crystal microbalance biosensor for prostate specific antigen detection. *Surf. Interfaces* **2024**, *45*, 103877. [CrossRef]
41. Yang, X.M.; Zhong, Z.W.; Diallo, E.M.; Wang, Z.H.; Yue, W.S. Silicon wafer wettability and aging behaviors: Impact on gold thin-film morphology. *Mater. Sci. Semicond. Process.* **2014**, *26*, 25–32. [CrossRef]
42. Sethi, J.; Suhail, A.; Safarzadeh, M.; Sattar, A.; Wei, Y.; Pan, G. NH2 linker for femtomolar label-free detection with reduced graphene oxide screen-printed electrodes. *Carbon* **2021**, *179*, 514–522. [CrossRef]
43. Latif, U.; Can, S.; Hayden, O.; Grillberger, P.; Dickert, F.L. Sauerbrey and anti-Sauerbrey behavioral studies in QCM sensors—Detection of bioanalytes. *Sens. Actuators B Chem.* **2013**, *176*, 825–830. [CrossRef]
44. Beyazit, F.; Arica, M.Y.; Acikgoz-Erkaya, I.; Ozalp, C.; Bayramoglu, G. Quartz crystal microbalance–based aptasensor integrated with magnetic pre-concentration system for detection of Listeria monocytogenes in food samples. *Microchim. Acta* **2024**, *191*, 235. [CrossRef] [PubMed]
45. Zubrytė, R.; Mavliutova, L.; García, Y.; Sullivan, M.V.; Turner, N.W.; Patitucci, F.; Polania, L.C.; Jiménez, V.A.; Porter, R.; Mattsson, A.; et al. Development of molecularly imprinted polymers for the detection of human chorionic gonadotropin. *Sci. Rep.* **2025**, *15*, 10436. [CrossRef] [PubMed]
46. Cuffaro, D.; Bonasera, L.; Nuti, E.; Galletti, R.; Adami, M.; Sartore, M.; Minunni, M. Development of an Improved QCM-D Instrumentation for Affinity Sensing by Bioinspired Molecular-Imprinted Polymers (MIP) for IgG Detection in Serum. *Sensors* **2026**, *26*, 2985. [CrossRef] [PubMed]
47. Rahman, M.A.; Pal, R.K.; Islam, N.; Freeman, R.; Berthiaume, F.; Mazzeo, A.; Ashraf, A. A Facile Graphene Conductive Polymer Paper Based Biosensor for Dopamine, TNF-α, and IL-6 Detection. *Sensors* **2023**, *23*, 8115. [CrossRef] [PubMed]
48. Olson, W.; Colasanti, A.; Lu, X.-J.; Zhurkin, V. Watson–Crick Base Pairs: Character and Recognition. In *Wiley Encyclopedia of Chemical Biology*; John Wiley & Sons: Hoboken, NJ, USA, 2008.
49. Resmi, A.N.; Rekha, C.R.; Emilia, P.; Kunnumpurathu, J.; Sivaselvam, S.; Praveen, C.S.; Emmanuel N, K.; Rerat, M.; Ramapurath S, J.; Panaghiotis, K. Molecular-Architectonics of Gold Nanoclusters for enhanced fluorescence and photosensitizing property for Image Guided Photodynamic Therapy of Hypoxic Tumor. *ChemRxiv* **2023**. [CrossRef]
50. Xue, Y.; Li, X.; Li, H.; Zhang, W. Quantifying thiol–gold interactions towards the efficient strength control. *Nat. Commun.* **2014**, *5*, 4348. [CrossRef] [PubMed]
51. Grey, L.H.; Nie, H.-Y.; Biesinger, M.C. Defining the nature of adventitious carbon and improving its merit as a charge correction reference for XPS. *Appl. Surf. Sci.* **2024**, *653*, 159319. [CrossRef]
52. Caprile, L.; Cossaro, A.; Falletta, E.; Della Pina, C.; Cavalleri, O.; Rolandi, R.; Terreni, S.; Ferrando, R.; Rossi, M.; Floreano, L.; et al. Interaction of l-cysteine with naked gold nanoparticles supported on HOPG: A high resolution XPS investigation. *Nanoscale* **2012**, *4*, 7727–7734. [CrossRef] [PubMed]
53. Vericat, C.; Vela, M.E.; Benitez, G.; Carro, P.; Salvarezza, R.C. Self-assembled monolayers of thiols and dithiols on gold: New challenges for a well-known system. *Chem. Soc. Rev.* **2010**, *39*, 1805–1834. [CrossRef] [PubMed]
54. Zhao, Y.; Zhou, F.; Zhou, H.; Su, H. The structural and bonding evolution in cysteine–gold cluster complexes. *Phys. Chem. Chem. Phys.* **2013**, *15*, 1690–1698. [CrossRef] [PubMed]
55. Ortega, M.; Tremont, R.; Vega, C.; López-Garriga, J. Electrochemistry of Hemoglobin I from Lucina pectinata immobilized on a modified gold electrode with 3-mercaptopropionic acid. *Int. J. Anal. Bioanal. Chem.* **2012**, *2*, 218–227.

56. Thébault, P.; Ammoun, M.; Boudjemaa, R.; Ouvrard, A.; Steenkeste, K.; Bourguignon, B.; Fontaine-Aupart, M.-P. Surface functionalization strategy to enhance the antibacterial effect of nisin Z peptide. *Surf. Interfaces* **2022**, *30*, 101822. [CrossRef]
57. Kumar, S.; Soni, S.; Danowski, W.; van Beek, C.L.F.; Feringa, B.L.; Rudolf, P.; Chiechi, R.C. Correlating the Influence of Disulfides in Monolayers across Photoelectron Spectroscopy Wettability and Tunneling Charge-Transport. *J. Am. Chem. Soc.* **2020**, *142*, 15075–15083. [CrossRef] [PubMed]
58. Tsai, S.-Y.; Liu, Y.-L. Preparation of Carbon Nanotube-Sulfur Nanohybrid Materials with Elemental Sulfur as a Feedstock. *ACS Omega* **2026**, *11*, 8678–8684. [CrossRef] [PubMed]
59. Omidiyan, M.; Tajalli, P.; Tran, H.-V.; Hoijang, S.; Lee, T.R. Siloxane-Terminated Self-Assembled Monolayers for Mimicking Nanoscale Hydrophobic Polydimethylsiloxane Surfaces. *Langmuir* **2025**, *41*, 33731–33738. [CrossRef] [PubMed]
60. Omidiyan, M.; Wang, M.; Tajalli, P.; He, X.; Hoijang, S.; Cai, C.; Chiang, N.; Lee, T.R. Gold–Silver Nanoshell-Embedded Polydimethylsiloxane Films for Near-Infrared Photothermal Eradication of Bacteria. *ACS Appl. Mater. Interfaces* **2025**, *17*, 64065–64076. [CrossRef] [PubMed]
61. Ge, L.; Trinh, T.K.H.; Li, C.; Mayer, F.; Chin, J.M.; Chen, C.-L.; Reithofer, M.R. Directed Synthesis of Gold Nanoparticle Superstructures Using Self-Assembling Peptoids Containing Metal-Bonding N-Heterocyclic Carbenes. *Nano Lett.* **2025**, *25*, 12049–12058. [CrossRef] [PubMed]
62. Castner, D.G.; Hinds, K.; Grainger, D.W. X-ray Photoelectron Spectroscopy Sulfur 2p Study of Organic Thiol and Disulfide Binding Interactions with Gold Surfaces. *Langmuir* **1996**, *12*, 5083–5086. [CrossRef]
63. Gonella, G.; Terreni, S.; Cvetko, D.; Cossaro, A.; Mattera, L.; Cavalleri, O.; Rolandi, R.; Morgante, A.; Floreano, L.; Canepa, M. Ultrahigh Vacuum Deposition of l-Cysteine on Au(110) Studied by High-Resolution X-ray Photoemission: From Early Stages of Adsorption to Molecular Organization. *J. Phys. Chem. B* **2005**, *109*, 18003–18009. [CrossRef] [PubMed]
64. Farkhondeh, H.; Rahsepar, F.R.; Zhang, L.; Leung, K.T. Structural and Chemical Evolution of l-Cysteine Nanofilm on Si(111)-$\sqrt{3}\times\sqrt{3}$-Ag: From Preferential Growth at Step Edges and Antiphase Boundaries at Room Temperature to Adsorbate-Mediated Metal Cluster Formation at Elevated Temperature. *Langmuir* **2019**, *35*, 16185–16200. [CrossRef] [PubMed]
65. Shin, T.; Kim, K.-N.; Lee, C.-W.; Shin, S.; Kang, H. Self-Assembled Monolayer of l-Cysteine on Au(111): Hydrogen Exchange between Zwitterionic l-Cysteine and Physisorbed Water. *J. Phys. Chem. B* **2003**, *107*, 11674–11681. [CrossRef]
66. Jürgensen, A.; Raschke, H.; Esser, N.; Hergenröder, R. An in situ XPS study of L-cysteine co-adsorbed with water on polycrystalline copper and gold. *Appl. Surf. Sci.* **2017**, *435*, 870–879. [CrossRef]
67. Cozzens, Y.; Wang, P.; Whitten, J.E. Adsorption of l-Cysteine and Cysteamine on Zinc Oxide Nanoparticles. *Langmuir* **2024**, *40*, 23538–23548. [CrossRef] [PubMed]
68. Hareesh, K.; Williams, J.F.; Dhole, N.A.; Kodam, K.M.; Bhoraskar, V.N.; Dhole, S.D. Bio-green synthesis of Ag–GO, Au–GO and Ag–Au–GO nanocomposites using Azadirachta indica: Its application in SERS and cell viability. *Mater. Res. Express* **2016**, *3*, 075010. [CrossRef]
69. Kariper, İ.A.; Çağlayan, M.O.; Üstündağ, Z. Heterogeneous Au/Ru hybrid nanoparticle decorated graphene oxide nanosheet catalyst for the catalytic reduction of nitroaromatics. *Res. Chem. Intermed.* **2019**, *45*, 801–813. [CrossRef]
70. Sah, D.; Surabhi; Gupta, P.; Shabir, J.; Dhama, M.; Mozumdar, S. Diamine-functionalized porous graphene oxide sheets decorated with palladium oxide nanoparticles for the oxidative amidation of aldehydes. *New J. Chem.* **2022**, *46*, 20828–20843. [CrossRef]
71. Chiticaru, E.A.; Damian, C.M.; Pilan, L.; Ioniță, M. Label-Free DNA Biosensor Based on Reduced Graphene Oxide and Gold Nanoparticles. *Biosensors* **2023**, *13*, 797. [CrossRef] [PubMed]
72. Dreyer, D.R.; Park, S.; Bielawski, C.W.; Ruoff, R.S. The chemistry of graphene oxide. *Chem. Soc. Rev.* **2010**, *39*, 228–240. [CrossRef] [PubMed]
73. Ederer, J.; Janoš, P.; Ecorchard, P.; Tolasz, J.; Štengl, V.; Beneš, H.; Perchacz, M.; Pop-Georgievski, O. Determination of amino groups on functionalized graphene oxide for polyurethane nanomaterials: XPS quantitation vs. functional speciation. *RSC Adv.* **2017**, *7*, 12464–12473. [CrossRef]
74. Hampitak, P.; Jowitt, T.A.; Melendrez, D.; Fresquet, M.; Hamilton, P.; Iliut, M.; Nie, K.; Spencer, B.; Lennon, R.; Vijayaraghavan, A. A Point-of-Care Immunosensor Based on a Quartz Crystal Microbalance with Graphene Biointerface for Antibody Assay. *ACS Sens.* **2020**, *5*, 3520–3532. [CrossRef] [PubMed]
75. Kol, S.; Kocaman Kabil, F.; Aydemir, N.; Oral, A.Y. Nanoarchitectonics in immobilization of DNT/TNT specific binding peptides on laser-induced graphene. *Mater. Res. Express* **2024**, *11*, 125102. [CrossRef]